

# Weak Adversarial Neural Pushforward Method for Fractional Fokker-Planck Equations

Andrew Qing He<sup>1</sup>      Wei Cai<sup>1</sup>

<sup>1</sup>Department of Mathematics, Southern Methodist University, Dallas, TX  
75275, USA

*Preprint — March 23, 2026*

## Abstract

We extend the Weak Adversarial Neural Pushforward Method (WANPM) to fractional Fokker-Planck equations, in which the classical Laplacian diffusion operator is replaced by the fractional Laplacian of order  $\alpha \in (0, 2]$ . The solution distribution is represented as the pushforward of a simple base distribution through a neural network, and the weak formulation is discretized entirely via Monte Carlo sampling without any temporal mesh. A key computational advantage is that plane-wave test functions are eigenfunctions of the fractional Laplacian, making the operator cost identical to that of classical diffusion for any  $\alpha$ . We validate the method on seven benchmark problems with  $\alpha = 1.5$ , spanning one and two spatial dimensions: the steady-state fractional Ornstein–Uhlenbeck (OU) process, a harmonic confining potential, a double-well potential, and a triple-well potential in one dimension, a steady-state 2D double-peak distribution, a time-dependent 2D ring distribution with rotational drift, and a five-dimensional harmonic potential. Each case is benchmarked against particle simulations using symmetric  $\alpha$ -stable Lévy increments, and robust statistics confirm close agreement throughout. The method is mesh-free, requires no density evaluation or non-local quadrature, and provides a promising foundation for high-dimensional anomalous diffusion solvers.

**Keywords:** fractional Fokker-Planck equation, fractional Laplacian, neural pushforward map, weak adversarial network, Lévy stable process, plane-wave test functions, anomalous diffusion.

**MSC (2020):** 65N75, 68T07, 35R11, 60G52.

## Contents

<b>1</b>	<b>Introduction</b>	<b>2</b>
<b>2</b>	<b>Fractional Fokker-Planck Equation and Its Weak Formulation</b>	<b>4</b>
2.1	Strong Form . . . . .	4
2.2	Steady-State Theory . . . . .	4
2.3	Weak Formulation of the Transient Problem . . . . .	5
2.4	Weak Formulation of the Steady-State Problem . . . . .	6
2.5	Eigenfunction Property of Plane-Wave Test Functions . . . . .	6

<b>3</b>	<b>Weak Adversarial Neural Pushforward Method</b>	<b>7</b>
3.1	Pushforward Network Architecture for the Transient Problem . . . . .	7
3.2	Pushforward Network Architecture for the Steady-State Problem . . . . .	7
3.3	Plane-Wave Test Functions . . . . .	8
3.4	Monte Carlo Discretisation of the Weak Form . . . . .	8
3.5	Adversarial Min-Max Training . . . . .	8
<b>4</b>	<b>Particle Simulation as Ground Truth</b>	<b>9</b>
4.1	Symmetric $\alpha$ -Stable Lévy Increments . . . . .	9
4.2	Why Robust Statistics Are Required . . . . .	10
<b>5</b>	<b>Numerical Results</b>	<b>10</b>
5.1	Experiment 1: Steady-State Ornstein–Uhlenbeck Process . . . . .	10
5.2	Experiment 2: Harmonic Confining Potential . . . . .	11
5.3	Experiment 3: Double-Well Potential . . . . .	14
5.4	Experiment 4: Triple-Well Potential . . . . .	16
5.5	Experiment 5: Steady-State 2D Double-Peak Distribution . . . . .	17
5.6	Experiment 6: Time-Dependent 2D Ring with Rotational Drift . . . . .	19
5.7	Experiment 7: Five-Dimensional Harmonic Potential . . . . .	19
<b>6</b>	<b>Discussion and Outlook</b>	<b>21</b>
6.1	Strengths of the Approach . . . . .	21
6.2	Comparison of the Seven Experiments . . . . .	22
6.3	Limitations and Caveats . . . . .	22
6.4	Relationship to the fBm Fokker-Planck Equation . . . . .	22
6.5	Future Directions . . . . .	23
<b>7</b>	<b>Conclusion</b>	<b>23</b>

# 1 Introduction

Fokker-Planck equations (FPEs) govern the evolution of probability density functions in stochastic dynamical systems and arise ubiquitously in statistical physics, chemistry, biology, and finance. Their classical form involves a second-order diffusion operator corresponding to Brownian noise; however, many natural phenomena exhibit anomalous diffusion driven by heavy-tailed Lévy processes rather than Gaussian noise. The appropriate PDE for such systems is the *fractional* Fokker-Planck equation (fFPE), in which the Laplacian diffusion term is replaced by the fractional Laplacian  $(-\Delta)^{\alpha/2}$  with  $\alpha \in (0, 2)$ . Fractional FPEs model superdiffusion in turbulent transport, charge carrier dynamics in amorphous semiconductors, and anomalous relaxation in complex fluids [1, 2].

Solving the fFPE in high dimensions poses formidable challenges. Classical finite-element or finite-difference discretisations of the fractional Laplacian require dense stiffness matrices whose assembly and storage become prohibitive even in modest dimensions. Spectral methods are effective in simple geometries but do not readily extend to curved or unbounded domains. Deep learning approaches, which have recently achieved remarkable success for classical high-dimensional PDEs, must contend with two additional obstacles in the fractional setting: (i) pointwise neural-network representations of the solution density require computing the fractional Laplacian of the network output, which involves

non-local integral operators and is expensive to evaluate; and (ii) the solution distribution may have heavy algebraic tails that a neural network density must resolve over an exponentially large effective domain.

In a companion paper [3] we introduced the Weak Adversarial Neural Pushforward Method (WANPM) for *classical* Fokker-Planck equations. The core idea is to represent the solution distribution as the pushforward of a tractable base distribution through a neural map  $F_{\theta}$ , and to train  $F_{\theta}$  adversarially against a family of plane-wave test functions so that the induced distribution satisfies the weak form of the FPE. This approach avoids explicit density evaluation, density normalisation, and second-order backpropagation through the solution network. The pushforward map  $F_{\theta}$  can take a base distribution of arbitrary dimension  $d$  as input and map it to the  $n$ -dimensional target space, providing representational flexibility that is particularly valuable for complex or heavy-tailed target distributions.

The present paper extends WANPM to the fractional setting. The extension is both natural and computationally efficient: because plane waves are eigenfunctions of the fractional Laplacian, the action of  $(-\Delta)^{\alpha/2}$  on any test function  $f^{(k)}(t, x) = \sin(\mathbf{w}^{(k)} \cdot \mathbf{x} + \kappa^{(k)}t + b^{(k)})$  reduces to multiplication by  $|\mathbf{w}^{(k)}|^{\alpha}$ —an  $\mathcal{O}(1)$  operation per test function. This eigenfunction property means that changing from classical diffusion ( $\alpha = 2$ ) to fractional diffusion ( $\alpha < 2$ ) requires only a single parameter change in the loss computation; no quadrature of the non-local kernel is necessary.

Our contributions are as follows.

1. We derive the weak formulations of both the time-dependent and steady-state ffPE and show how they can be evaluated as Monte Carlo expectations with respect to the pushforward distribution, without discretising time.
2. We establish the theoretical steady-state distribution for the fractional Ornstein–Uhlenbeck process and its connection to  $\alpha$ -stable laws, and describe the fractional Laplacian eigenfunction property that makes plane-wave test functions exact and computationally efficient for the fractional operator.
3. We implement and validate the method on seven benchmark problems with  $\alpha = 1.5$ : the fractional Ornstein–Uhlenbeck steady state, a harmonic confining potential, a double-well potential, and a triple-well potential in one dimension; a steady-state 2D double-peak distribution; a time-dependent 2D ring distribution with rotational drift; and a five-dimensional harmonic potential.
4. We demonstrate that robust statistics—median, interquartile range (IQR), median absolute deviation (MAD), and percentile bands—are the appropriate comparison metrics for heavy-tailed distributions, and that standard deviation is unreliable for  $\alpha < 2$ .

The remainder of the paper is organized as follows. Section 2 presents the fractional Fokker-Planck equation, the steady-state theory, and the weak formulations for both the transient and steady-state problems. Section 3 describes the neural pushforward architecture and the adversarial training procedure. Section 4 presents the particle simulation used as a ground-truth benchmark. Section 5 reports the seven numerical experiments. Section 6 discusses limitations and future directions.

## 2 Fractional Fokker-Planck Equation and Its Weak Formulation

### 2.1 Strong Form

Let  $X_t$  be a stochastic process on  $\mathbb{R}$  satisfying the Itô SDE

$$dX_t = b(X_t) dt + dL_t^{(\alpha)}, \quad X_0 \sim \rho_0, \quad (1)$$

where  $b : \mathbb{R} \rightarrow \mathbb{R}$  is a drift coefficient and  $L_t^{(\alpha)}$  is a symmetric  $\alpha$ -stable Lévy process with characteristic exponent  $\mathbb{E}[e^{i\xi L_t}] = e^{-t|\xi|^\alpha}$ . For  $\alpha = 2$  this reduces to standard Brownian motion with diffusivity 1. The probability density  $\rho(x, t)$  of  $X_t$  satisfies the fractional Fokker-Planck equation

$$\frac{\partial \rho}{\partial t} + (-\Delta_x)^{\alpha/2} \rho + \frac{\partial}{\partial x} [b(x)\rho] = 0, \quad (x, t) \in \mathbb{R} \times (0, T], \quad (2)$$

with initial condition  $\rho(x, 0) = \rho_0(x)$ . Here  $(-\Delta_x)^{\alpha/2}$  is the Riesz fractional Laplacian, defined spectrally by

$$\widehat{(-\Delta)^{\alpha/2} u}(\xi) = |\xi|^\alpha \hat{u}(\xi),$$

where  $\hat{u}$  denotes the Fourier transform. Equation (2) conserves probability:  $\int_{\mathbb{R}} \rho(x, t) dx = 1$  for all  $t \geq 0$ .

For the numerical experiments of this paper we always take  $\alpha = 1.5$ , so that the fractional Laplacian  $(-\Delta)^{3/4}$  lies strictly between the first-order and the classical second-order differential operators in terms of its smoothing properties. The solution develops algebraically decaying tails characteristic of  $\alpha$ -stable distributions, in contrast to the Gaussian tails arising in the classical ( $\alpha = 2$ ) case.

**Remark 1** (Normalisation convention). *Our convention sets the coefficient of  $(-\Delta)^{\alpha/2}$  to unity, so the characteristic function of the Lévy increment over a unit time interval is  $e^{-|\xi|^\alpha}$ . The fractional diffusion coefficient can be absorbed into the wavenumber normalisation of the test functions without loss of generality.*

### 2.2 Steady-State Theory

When the drift is the negative gradient of a confining potential,  $b(x) = -V'(x)$ , and the process is ergodic, equation (2) admits a unique steady-state distribution  $\rho_\infty$  satisfying

$$(-\Delta_x)^{\alpha/2} \rho_\infty + \frac{d}{dx} [b(x)\rho_\infty] = 0. \quad (3)$$

We now establish the steady-state distribution analytically for the linear (Ornstein–Uhlenbeck) case, and explain why no analogous closed form exists for nonlinear drifts.

**Fractional Ornstein–Uhlenbeck steady state.** For the linear drift  $b(x) = -\theta(x - \mu)$  with  $\theta > 0$ , the SDE (1) is the fractional Ornstein–Uhlenbeck (fOU) process. Taking the Fourier transform of (3) and using  $\widehat{(-\Delta)^{\alpha/2} u} = |\xi|^\alpha \hat{u}$  together with  $\partial_x \widehat{[(x - \mu)\rho_\infty]}(\xi) = -i\partial_\xi [\xi \hat{\rho}_\infty] + i\mu \xi \hat{\rho}_\infty$  yields (after shifting to  $\mu = 0$  for clarity)

$$|\xi|^\alpha \hat{\rho}_\infty(\xi) = -\theta \frac{\partial}{\partial \xi} [\xi \hat{\rho}_\infty(\xi)]. \quad (4)$$

This is a first-order linear ODE in  $\xi$ . Substituting the  $\alpha$ -stable ansatz  $\hat{\rho}_\infty(\xi) = e^{-c^\alpha|\xi|^\alpha}$  into (4) gives

$$c^\alpha|\xi|^\alpha e^{-c^\alpha|\xi|^\alpha} = \theta(1 + \alpha c^\alpha|\xi|^\alpha) e^{-c^\alpha|\xi|^\alpha},$$

which is satisfied for all  $\xi$  if and only if  $c^\alpha = 1/(2\theta)$ , i.e.  $c = (2\theta)^{-1/\alpha}$ . Hence

$$\log \hat{\rho}_\infty(\xi) = -\frac{|\xi|^\alpha}{2\theta}. \quad (5)$$

**Proposition 1** (Fractional OU steady state). *For the fOU process with drift  $b(x) = -\theta(x - \mu)$ ,  $\theta > 0$ , and stability index  $\alpha \in (0, 2)$ , the unique steady-state distribution is the symmetric  $\alpha$ -stable law  $S_\alpha((2\theta)^{-1/\alpha}, 0, \mu)$ , whose characteristic function is*

$$\hat{\rho}_\infty(\xi) = \exp\left(-\frac{|\xi|^\alpha}{2\theta}\right) e^{i\mu\xi}.$$

For  $\alpha = 2$  this reduces to the Gaussian  $\mathcal{N}(\mu, 1/(2\theta))$ .

The density of  $S_\alpha((2\theta)^{-1/\alpha}, 0, \mu)$  has no elementary closed form for general  $\alpha \in (0, 2)$ , but its tail behavior is known analytically [5]:

$$\rho_\infty(x) \sim \frac{C_\alpha}{(2\theta)|x - \mu|^{1+\alpha}} \quad \text{as } |x - \mu| \rightarrow \infty, \quad (6)$$

for an explicit constant  $C_\alpha > 0$ . In particular, the distribution has infinite variance for all  $\alpha < 2$ , which is the hallmark of anomalous diffusion and motivates our use of robust statistics rather than second-moment comparisons in Section 5.

**General gradient drift.** For a non-linear gradient drift  $b(x) = -V'(x)$ , no closed-form steady state is available for  $\alpha < 2$ . In the classical case ( $\alpha = 2$ , standard Brownian driving noise with diffusivity  $\sigma^2/2$ ), the steady state is the Boltzmann distribution  $\rho_\infty(x) \propto \exp(-V(x)/(\sigma^2/2))$ . This explicit formula arises because the detailed-balance condition can be integrated exactly to cancel the drift and diffusion contributions. For  $\alpha < 2$ , detailed balance takes the Fourier-space form

$$|\xi|^\alpha \hat{\rho}_\infty(\xi) = i\xi \widehat{b \cdot \rho_\infty}(\xi), \quad (7)$$

which is a non-local integral equation coupling all frequency modes through the convolution  $\widehat{b \cdot \rho_\infty}$ . No general closed-form inversion is known for non-linear  $b$ , which is precisely why neural methods benchmarked against long-time particle simulations are valuable for studying fractional steady-state distributions.

## 2.3 Weak Formulation of the Transient Problem

Let  $f(t, x)$  be a smooth test function decaying sufficiently rapidly as  $|x| \rightarrow \infty$ . Multiplying (2) by  $f$  and integrating by parts in both space and time over  $\mathbb{R} \times [0, T]$  yields

$$\mathbb{E}_{\rho(T, \cdot)}[f(T, \cdot)] - \mathbb{E}_{\rho_0}[f(0, \cdot)] - \int_0^T \mathbb{E}_{\rho(t, \cdot)} \left[ \frac{\partial f}{\partial t} + \mathcal{L}f \right] dt = 0, \quad (8)$$

where the operator  $\mathcal{L}$  acts on the test function by

$$\mathcal{L}f = -(-\Delta_x)^{\alpha/2} f + b(x) \frac{\partial f}{\partial x}. \quad (9)$$

The fractional term  $(-\Delta_x)^{\alpha/2} f$  is well-defined for any smooth  $f$  via the Fourier identity  $|\xi|^\alpha \hat{f}$ , and the integration-by-parts step is valid whenever  $\rho$  has sufficient integrability.

**Remark 2** (Structure of the weak form). *Equation (8) decomposes into three Monte Carlo-evaluable expectations: a terminal expectation at  $t = T$ , an initial-condition expectation at  $t = 0$  (which can be computed from samples of  $\rho_0$  independently of the learned network), and an interior expectation integrated uniformly over  $[0, T]$ . This three-term structure is identical to that of the classical FPE [3] up to the replacement of  $-\partial^2/\partial x^2$  by  $(-\Delta_x)^{\alpha/2}$  in the operator  $\mathcal{L}$ . In particular, the fractional and classical problems have the same computational graph; only the scalar multiplier  $|\mathbf{w}|^\alpha$  in the loss changes with  $\alpha$ .*

## 2.4 Weak Formulation of the Steady-State Problem

For the steady-state problem (3), multiplying by a smooth test function  $f(x)$  and integrating by parts yields the stationarity condition

$$\mathbb{E}_{\rho_\infty}[\mathcal{L}_{\text{ss}}f] = 0 \quad \text{for all smooth } f, \quad (10)$$

where the adjoint operator on the test function is

$$\mathcal{L}_{\text{ss}}f(x) = -(-\Delta_x)^{\alpha/2}f(x) + b(x)\frac{df}{dx}. \quad (11)$$

For sinusoidal test functions  $f(x) = \sin(wx + b)$ , this becomes

$$\mathcal{L}_{\text{ss}}f(x) = -|w|^\alpha \sin(wx + b) + b(x)w \cos(wx + b), \quad (12)$$

where the fractional term reduces to a simple scalar multiplication via the eigenfunction property. The adversarial training objective is then

$$\min_{\boldsymbol{\vartheta}} \max_{\{w^{(k)}, b^{(k)}\}} \frac{1}{K} \sum_{k=1}^K \left( \mathbb{E}_{\rho_{\boldsymbol{\vartheta}}} [\mathcal{L}_{\text{ss}}f^{(k)}] \right)^2, \quad (13)$$

where  $\rho_{\boldsymbol{\vartheta}} = G_{\boldsymbol{\vartheta}\#}\pi_{\text{base}}$  is the distribution of the pushforward samples.

## 2.5 Eigenfunction Property of Plane-Wave Test Functions

A spatial plane wave  $\phi_{\mathbf{w}}(x) = \sin(\mathbf{w} \cdot x + \varphi)$  satisfies

$$(-\Delta_x)^{\alpha/2}\phi_{\mathbf{w}}(x) = |\mathbf{w}|^\alpha\phi_{\mathbf{w}}(x), \quad (14)$$

which follows immediately from the Fourier-space definition of the fractional Laplacian. This identity is exact for all  $\alpha \in (0, 2]$  and all wavenumbers  $\mathbf{w}$ . In particular, for  $\alpha = 2$ , it reduces to  $-\partial^2\phi_{\mathbf{w}}/\partial x^2 = |\mathbf{w}|^2\phi_{\mathbf{w}}$ , consistent with classical differentiation.

The practical consequence is that the fractional part of  $\mathcal{L}f^{(k)}$  costs nothing extra to evaluate compared with classical diffusion: it is simply a multiplication by the scalar  $|\mathbf{w}^{(k)}|^\alpha$ . The entire ffPE loss computation therefore has the same computational complexity as the classical FPE loss, regardless of  $\alpha$ . This is the key property that makes the plane-wave test function choice especially attractive for fractional operators.

## 3 Weak Adversarial Neural Pushforward Method

### 3.1 Pushforward Network Architecture for the Transient Problem

We represent the solution distribution at each time  $t$  not by an explicit density but by a neural pushforward map

$$F_{\mathfrak{g}} : [0, T] \times \mathbb{R}^n \times \mathbb{R}^d \rightarrow \mathbb{R}^n, \quad (15)$$

where  $n = 1$  in our experiments and  $d$  is the dimension of a latent base distribution. Given  $x_0 \sim \rho_0$  and  $\mathbf{r} \sim \mathcal{N}(0, I_d)$ , the pushforward sample at time  $t$  is  $x(t) = F_{\mathfrak{g}}(t, x_0, \mathbf{r})$ . The induced distribution of  $x(t)$  is the learned approximation to  $\rho(\cdot, t)$ .

To enforce the initial condition exactly and to match the short-time diffusive scaling of Lévy processes, we parametrize

$$F_{\mathfrak{g}}(t, x_0, \mathbf{r}) = x_0 + \sqrt{t} \tilde{F}_{\mathfrak{g}}(t, x_0, \mathbf{r}), \quad (16)$$

where  $\tilde{F}_{\mathfrak{g}} : \mathbb{R}^{1+n+d} \rightarrow \mathbb{R}^n$  is a fully connected feedforward network with three hidden layers of width 128 and Tanh activation functions. At  $t = 0$ , the map reduces to the identity on  $x_0$ , so  $F_{\mathfrak{g}}(0, x_0, \mathbf{r}) = x_0 \sim \rho_0$  for any values of the network parameters—the initial condition is satisfied exactly by construction, with no penalisation term required in the loss. The  $\sqrt{t}$  prefactor is appropriate for diffusion-driven processes: the typical displacement of an  $\alpha$ -stable Lévy process over time  $t$  scales as  $t^{1/\alpha}$ , and for  $\alpha$  near 2 (and exactly for  $\alpha = 2$ ) this is well-approximated by  $\sqrt{t}$  at short times.

The base distribution dimension  $d$  can be chosen larger than the target dimension  $n$ , providing additional representational capacity without requiring Jacobian-determinant computations. In our experiments we use  $d = 5$  for the harmonic and steady-state cases, and  $d = 8$  for the double-well and triple-well cases where the target distribution is multimodal.

### 3.2 Pushforward Network Architecture for the Steady-State Problem

For the steady-state problem, the pushforward network has no time input and reduces to a map  $G_{\mathfrak{g}} : \mathbb{R}^d \rightarrow \mathbb{R}^n$ , parametrized simply as

$$G_{\mathfrak{g}}(\mathbf{r}) = \tilde{G}_{\mathfrak{g}}(\mathbf{r}), \quad (17)$$

where  $\tilde{G}_{\mathfrak{g}}$  is a fully connected feedforward network with three hidden layers of width 128 and Tanh activations, and  $\mathbf{r} \sim \mathcal{N}(0, I_d)$ . Because there is no initial condition to enforce, no  $\sqrt{t}$  prefactor is needed, and the network is free to map the Gaussian base distribution to any target shape, including heavy-tailed  $\alpha$ -stable distributions.

**Remark 3** (Overparameterised base distributions). *Allowing the base dimension  $d > n$  precludes the use of invertible (normalizing flow) architectures, which require  $d = n$  for the change-of-variables formula to hold. This is not a limitation but a feature: the extra latent dimensions provide additional representational capacity without requiring Jacobian-determinant computations. For heavy-tailed targets such as  $\alpha$ -stable distributions, invertible architectures with  $d = n$  may be insufficient, while the overparameterised pushforward can allocate multiple latent directions to represent different features of the tail.*

### 3.3 Plane-Wave Test Functions

We parametrize the test functions as full space-time plane waves,

$$f^{(k)}(t, x) = \sin(w^{(k)}x + \kappa^{(k)}t + b^{(k)}), \quad k = 1, \dots, K, \quad (18)$$

where  $w^{(k)} \in \mathbb{R}$ ,  $\kappa^{(k)} \in \mathbb{R}$ , and  $b^{(k)} \in \mathbb{R}$  are trainable parameters. The derivatives required by the weak form (8) and the operator (9) are all available in closed form:

$$\frac{\partial f^{(k)}}{\partial t}(t, x) = \kappa^{(k)} \cos(w^{(k)}x + \kappa^{(k)}t + b^{(k)}), \quad (19)$$

$$\frac{\partial f^{(k)}}{\partial x}(t, x) = w^{(k)} \cos(w^{(k)}x + \kappa^{(k)}t + b^{(k)}), \quad (20)$$

$$(-\Delta_x)^{\alpha/2} f^{(k)}(t, x) = |w^{(k)}|^\alpha f^{(k)}(t, x), \quad (21)$$

where the last identity uses the eigenfunction property (14). No automatic differentiation through the test function is required. The operator (9) evaluated on the test function is therefore

$$\mathcal{L}f^{(k)}(t, x) = -|w^{(k)}|^\alpha f^{(k)}(t, x) + b(x) w^{(k)} \cos(w^{(k)}x + \kappa^{(k)}t + b^{(k)}). \quad (22)$$

For the steady-state case, the same formula holds with  $\kappa^{(k)} = 0$  and the time variable dropped.

### 3.4 Monte Carlo Discretisation of the Weak Form

The three terms in the weak residual (8) are each approximated by Monte Carlo estimates. We sample  $M_T$  terminal tuples  $(x_0, \mathbf{r})$  with  $x_0 \sim \rho_0$  and  $\mathbf{r} \sim \mathcal{N}(0, I_d)$  to form  $\hat{E}_T^{(k)}$ ;  $M_0$  initial samples  $\tilde{x}^{(i)} \sim \rho_0$  to form  $\hat{E}_0^{(k)}$ ; and  $M$  interior triples  $(t^{(m)}, x_0^{(m)}, \mathbf{r}^{(m)})$  with  $t^{(m)} \sim \mathcal{U}[\epsilon, T]$ ,  $x_0^{(m)} \sim \rho_0$ ,  $\mathbf{r}^{(m)} \sim \mathcal{N}(0, I_d)$  to form  $\hat{E}^{(k)}$ . The factor  $T$  in the interior estimate accounts for the uniform measure over  $[0, T]$ .

For each test function  $k$ , the weak-form residual is

$$R^{(k)} = \hat{E}_T^{(k)} - \hat{E}_0^{(k)} - \hat{E}^{(k)}, \quad (23)$$

and the total training loss is

$$\mathcal{L}(\boldsymbol{\vartheta}, \{\boldsymbol{\eta}^{(k)}\}) = \frac{1}{K} \sum_{k=1}^K (R^{(k)})^2, \quad (24)$$

where  $\boldsymbol{\eta}^{(k)} = \{w^{(k)}, \kappa^{(k)}, b^{(k)}\}$  are the test function parameters. For the steady-state problem, the same loss is used but with  $R^{(k)} = \hat{E}_{\text{ss}}^{(k)}$ , the single Monte Carlo estimate of  $\mathbb{E}_{\rho_\infty}[\mathcal{L}_{\text{ss}} f^{(k)}]$ .

### 3.5 Adversarial Min-Max Training

The pushforward network and the test functions are trained adversarially:

$$\min_{\boldsymbol{\vartheta}} \max_{\{\boldsymbol{\eta}^{(k)}\}} \mathcal{L}(\boldsymbol{\vartheta}, \{\boldsymbol{\eta}^{(k)}\}). \quad (25)$$

The generator (pushforward network) is updated by gradient descent to minimize the loss, improving the pushforward map to satisfy the weak form for the current set of test functions. The adversary (test function parameters) is updated by gradient ascent to maximize the loss, searching for the plane-wave modes that are hardest to satisfy. This adaptive mechanism concentrates the test-function basis on the frequency regime where the current learned distribution most severely violates the weak form.

The full procedure is summarized in Algorithm 1.

---

**Algorithm 1** Weak Adversarial Neural Pushforward for fFPE

---

- 1: **Input:**  $K, M, M_0, M_T, N_{\text{epochs}}, \alpha, T, \rho_0$
  - 2: **Initialise:** pushforward network  $F_{\boldsymbol{\vartheta}}$ ; test function parameters  $\boldsymbol{\eta} = \{w^{(k)}, \kappa^{(k)}, b^{(k)}\}_{k=1}^K$  randomly
  - 3: Optimisers: Adam (lr =  $10^{-3}$ ) for  $\boldsymbol{\vartheta}$ ; Adam (lr =  $10^{-2}$ ) for  $\boldsymbol{\eta}$
  - 4: **for** epoch =  $1, \dots, N_{\text{epochs}}$  **do**
  - 5:     Sample  $(t^{(m)}, x_0^{(m)}, \mathbf{r}^{(m)})$ ,  $\tilde{x}^{(i)}$ ,  $(x_0^T, \mathbf{r}^T)$  from respective distributions
  - 6:     Compute  $\mathcal{L}(\boldsymbol{\vartheta}, \boldsymbol{\eta})$  via (24)
  - 7:     Update  $F_{\boldsymbol{\vartheta}}$ :  $\boldsymbol{\vartheta} \leftarrow \boldsymbol{\vartheta} - \nabla_{\boldsymbol{\vartheta}} \mathcal{L}$  ▷ gradient descent on generator
  - 8:     Update adversarial test functions:  $\boldsymbol{\eta} \leftarrow \boldsymbol{\eta} + \nabla_{\boldsymbol{\eta}} \mathcal{L}$  ▷ gradient ascent on test functions
  - 9: **end for**
- 

In practice, the learning rate for the generator is decayed using cosine annealing, and gradient clipping with maximum norm 1.0 is applied to both the generator and adversary parameter updates. The two updates may be performed with different frequencies in practice (e.g. multiple adversary steps per generator step) to stabilize the adversarial dynamics, as discussed in [3].

## 4 Particle Simulation as Ground Truth

For  $\alpha < 2$ , no closed-form analytical solution for the density  $\rho(x, t)$  of equation (2) is available in the presence of a non-trivial drift. We therefore benchmark the neural solution against a particle simulation of the SDE (1).

### 4.1 Symmetric $\alpha$ -Stable Lévy Increments

The characteristic function of a symmetric  $\alpha$ -stable distribution with unit scale is  $e^{-|\xi|^\alpha}$ . Over a time step  $\Delta t$ , the SDE increment  $\Delta L^{(\alpha)}$  has scale  $(\Delta t)^{1/\alpha}$ . We generate increments using the Chambers-Mallows-Stuck algorithm [4] with  $\beta = 0$  (symmetry) and scale  $(\Delta t)^{1/\alpha}$ , implemented via `scipy.stats.levy_stable.rvs`. The Euler-Maruyama discretisation of (1) reads

$$X_{n+1} = X_n + b(X_n)\Delta t + \Delta L_n^{(\alpha)}, \quad (26)$$

with time step  $\Delta t = 0.01$  and  $N_{\text{particles}} = 10,000$ . For the steady-state benchmarks, we run the SDE for a sufficiently long time  $T_{\text{SDE}} = 50$  until the empirical distribution has converged to stationarity, as verified by checking that successive time-window histograms agree to within sampling noise.

## 4.2 Why Robust Statistics Are Required

For  $\alpha < 2$ , symmetric  $\alpha$ -stable distributions have infinite variance. In finite-sample particle simulations, the empirical variance fluctuates wildly from run to run due to rare but large excursions, making the standard deviation an unreliable comparison metric. Specifically, for a sample of  $N$  i.i.d. observations from an  $\alpha$ -stable law with  $\alpha < 2$ , the sample variance does not converge as  $N \rightarrow \infty$ ; instead it grows at rate  $N^{2/\alpha-1}$  by the generalized central limit theorem [5].

We therefore rely exclusively on the following robust statistics for all quantitative comparisons in Section 5: the *median* as a measure of central tendency; the *interquartile range* (IQR) as a measure of spread; the *median absolute deviation* (MAD) as a scale estimate; and *percentile bands* (10th–90th) to summarize the bulk of the distribution. All of these quantities are well-defined and have finite-sample estimators that converge even for  $\alpha$ -stable distributions with  $\alpha < 2$ .

## 5 Numerical Results

We present seven benchmark experiments, all with  $\alpha = 1.5$ . In each case, the pushforward network uses a fully connected architecture with three hidden layers of width 128 and Tanh activations (four layers for the 2D ring experiment). The Adam optimizer is used with learning rate  $10^{-3}$  for the generator and  $10^{-2}$  for the test functions. The generator learning rate is decayed by cosine annealing, and gradient clipping with maximum norm 1.0 is applied throughout. The experiments are presented in order of increasing difficulty and dimension: we begin with one-dimensional steady-state and transient problems, then extend to two-dimensional steady-state and transient problems, and finally to a five-dimensional transient problem.

Table 1: Summary of numerical experiments ( $\alpha = 1.5$  throughout).  $V$ : potential;  $T$ : time horizon (SDE run time for steady-state benchmarks);  $K$ : number of test functions;  $d$ : base dimension;  $N_p$ : particle count. The 2D double-peak potential is given in (29).

Experiment	$V$	$T$	$K$	$d$	Epochs	$N_p$
1D OU (steady)	$\frac{\theta}{2}(x - \mu)^2$	50	200	5	3000	10000
1D Harmonic (transient)	$\frac{1}{2}x^2$	2.0	2000	5	1000	10000
1D Double-well (transient)	$(x^2 - 1)^2$	2.0	3000	8	10000	10000
1D Triple-well (transient)	$x^2(x^2 - 1)^2$	2.5	2000	8	5000	10000
2D Double-peak (steady)	see (29)	20 (SDE)	300	8	10000	10000
2D Ring (transient)	$\frac{1}{4}(r^2 - r_0^2)^2$	0.5	300	8	5000	10000
5D Harmonic (transient)	$\frac{1}{2}\ \mathbf{x}\ ^2$	1.0	2000	5	500	10000

### 5.1 Experiment 1: Steady-State Ornstein–Uhlenbeck Process

**Problem setup.** We consider the fOU process with drift  $b(x) = -\theta(x - \mu)$ ,  $\theta = 1$ ,  $\mu = 2$ , and apply the steady-state formulation of Sections 2.2–2.4. By Proposition 1, the exact steady-state distribution is the symmetric  $\alpha$ -stable law  $S_{1.5}((2\theta)^{-1/1.5}, 0, 2)$  with scale parameter

$$c = (2\theta)^{-1/\alpha} = 2^{-1/1.5} = 2^{-2/3} \approx 0.630.$$

This distribution has no closed-form density expression but is characterized entirely by its characteristic function (5). Its tails decay algebraically as  $|x - 2|^{-2.5}$  by (6), so the distribution has infinite variance, and standard deviation is not an appropriate comparison metric.

**Training configuration.** The steady-state pushforward network  $G_{\theta} : \mathbb{R}^5 \rightarrow \mathbb{R}$  has no time input (see Section 3.2). It maps  $\mathbf{r} \sim \mathcal{N}(0, I_5)$  to samples from  $\rho_{\infty}$ . We use  $K = 200$  sinusoidal test functions  $f^{(k)}(x) = \sin(w^{(k)}x + b^{(k)})$ , with spatial frequencies  $w^{(k)}$  initialized from  $\mathcal{N}(0, 1)$  and phase offsets from  $\mathcal{U}[0, 2\pi]$ . The batch size for the Monte Carlo expectation in (10) is  $M = 2,000$  samples. The model is trained for 3,000 epochs. The particle benchmark uses 10,000 trajectories of the fOU SDE (26) integrated over  $T_{\text{SDE}} = 50$  time units at  $\Delta t = 0.01$ .

**Results.** Figure 1 shows the learned steady-state distribution alongside the particle benchmark histogram. The learned distribution closely matches the particle histogram across the full displayed support  $[-2, 6]$ , reproducing both the location of the peak near  $\mu = 2$  and the asymmetric heavy-tailed character of the particle histogram. The heavier right tail visible in the particle benchmark is consistent with the algebraic decay (6): with 10,000 particles, occasional large excursions skew the empirical histogram, and the learned distribution correctly reproduces the bulk of the distribution while the finite-sample tails fluctuate between runs.

The training loss, shown in the right panel of Figure 1, converges smoothly from an initial value of order  $10^0$  to below  $10^{-2}$  within roughly 500 epochs, after which it stabilizes with the adversarial oscillations characteristic of min-max training. The low number of test functions ( $K = 200$ ) and short training (3,000 epochs) is sufficient for this one-dimensional steady-state problem, reflecting the simplicity of the objective compared with the transient problems below.

This experiment also serves as a validation of the theoretical result in Proposition 1: by fitting the learned distribution to the known  $\alpha$ -stable law characterized by (5), one could in principle estimate  $\alpha$  and  $\theta$  from the pushforward samples without access to the SDE, demonstrating the method’s potential as a tool for statistical inference in fractional diffusion systems.

## 5.2 Experiment 2: Harmonic Confining Potential

**Problem setup.** We solve the transient ffPE (2) with the quadratic drift  $b(x) = -kx$ ,  $k = 1$ , on the time interval  $[0, 2]$ . The potential is  $V(x) = \frac{1}{2}x^2$ , with a single minimum at  $x = 0$ . The initial condition is a Gaussian centered at  $x_0 = 1.0$  with standard deviation  $\sigma_0 = 0.3$ ,

$$\rho_0(x) = \mathcal{N}(x; 1.0, 0.09), \quad (27)$$

offset from the potential minimum so that the dynamics are non-trivial: the drift carries the bulk of the distribution toward the origin while the fractional diffusion progressively develops heavy algebraic tails. This is the fractional analog of the classical Ornstein–Uhlenbeck transient problem, for which the  $\alpha = 2$  solution is a Gaussian with analytically trackable mean and variance. For  $\alpha = 1.5$ , no closed-form solution is available, and we benchmark against particle simulation. Figure 2 shows the potential and the initial density.

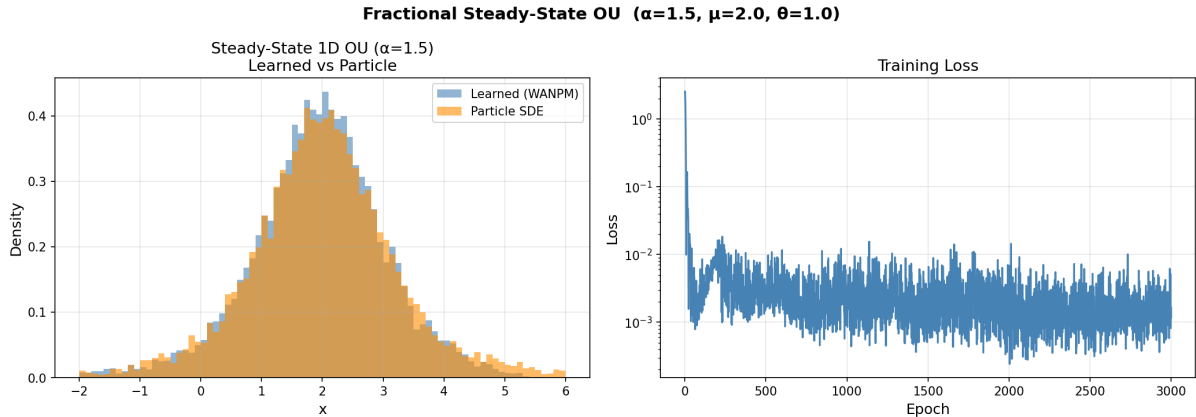


Figure 1: Steady-state fractional OU ( $\alpha = 1.5, \theta = 1, \mu = 2$ ): learned distribution (blue, WANPM) versus particle benchmark (orange, 10,000 particles,  $T_{\text{SDE}} = 50$ ). The theoretical steady state is the symmetric  $\alpha$ -stable law  $S_{1.5}(2^{-2/3}, 0, 2)$  (Proposition 1) with no closed-form density. The learned distribution faithfully captures the heavy-tailed  $\alpha$ -stable shape centered at  $\mu = 2$ . *Right*: training loss on a log scale, 3,000 epochs.

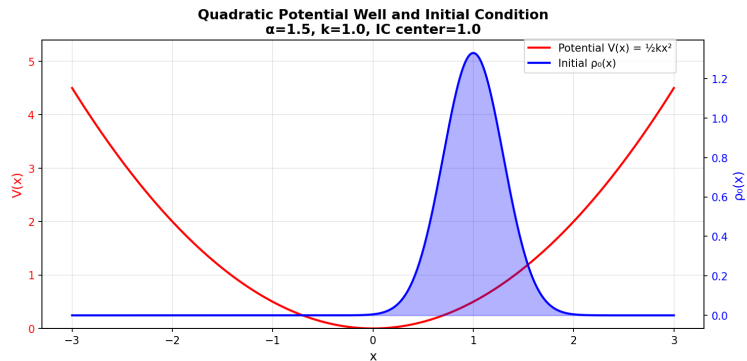


Figure 2: Quadratic confining potential  $V(x) = \frac{1}{2}kx^2$  (red, left axis) and initial condition  $\rho_0 = \mathcal{N}(1.0, 0.09)$  (blue, right axis),  $\alpha = 1.5, k = 1$ . The initial mass is offset from the potential minimum at  $x = 0$ ; the dynamics transport it toward the origin while fractional diffusion develops algebraically heavy tails.

**Training configuration.** The pushforward network uses base dimension  $d = 5$  and is trained with  $K = 2,000$  plane-wave test functions. The spatial frequencies  $w^{(k)}$  are initialized from  $\mathcal{N}(0, I)$  and normalized to unit norm; the temporal frequencies  $\kappa^{(k)}$  are drawn from  $\mathcal{N}(0, I)$ ; the phase offsets  $b^{(k)}$  are sampled from  $\mathcal{U}[0, 2\pi]$ . Batch sizes are  $M = 2,000$  for the interior term and  $M_0 = M_T = 1,000$  for the boundary terms. The model is trained for 1,000 epochs with cosine annealing.

**Training convergence.** Figure 3 shows the training loss and weak-form residual norm on log-scale axes over the 1,000 training epochs. Both curves exhibit a sharp initial descent spanning more than two orders of magnitude within the first 50 epochs, followed by a stabilisation phase in which the loss oscillates around approximately  $10^{-2}$ . The oscillatory behavior is characteristic of adversarial min-max training: the test functions periodically find harder frequency modes to probe, causing transient spikes in the loss that the generator then suppresses. The overall convergence is stable and monotonically decreasing on a moving average, confirming that the adversarial dynamics do not lead to

mode collapse or divergence.

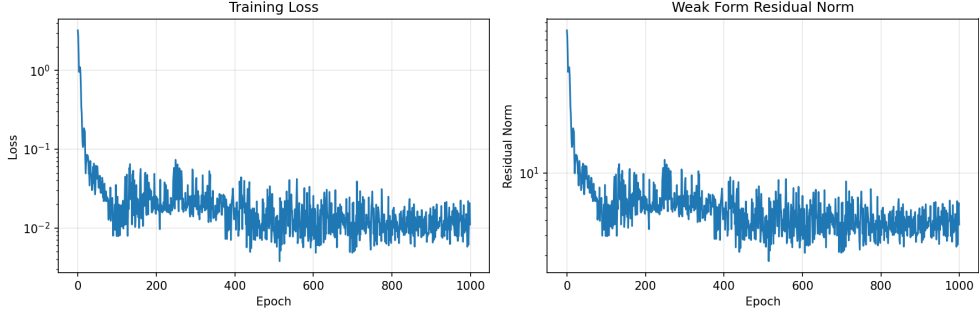


Figure 3: Training history for the harmonic fFPE ( $\alpha = 1.5$ , 1,000 epochs). *Left*: training loss (24) on a log scale. *Right*:  $\ell^2$  norm of the weak-form residual vector ( $R^{(1)}, \dots, R^{(K)}$ ) on a log scale (summed over  $K = 2,000$  modes). Both stabilize near  $10^{-2}$  after rapid initial descent.

**Transient distribution comparison.**

Figure 4 shows density-normalized histograms of 5,000 pushforward samples (blue) and 10,000 particle-simulation trajectories (green) at eight evenly-spaced times  $t \in \{0.0, 0.2, 0.4, 0.6, 0.8, 1.0, 1.5, 2.0\}$ . Both histograms are normalized over  $[-3, 3]$  with 100 bins. At  $t = 0$  both reproduce the initial Gaussian centered at  $x = 1.0$  accurately. As time evolves, the distribution drifts toward  $x = 0$  and develops the characteristic broad, algebraically decaying tails of  $\alpha$ -stable diffusion. The pushforward network faithfully tracks this evolution throughout, capturing both the shift in the bulk of the distribution and the progressive growth of the tails. By  $t = 1.5$  and  $t = 2.0$  the distribution has largely relaxed toward the fractional quasi-steady state, and the agreement between the learned distribution and the particle simulation remains good across the full visible support.

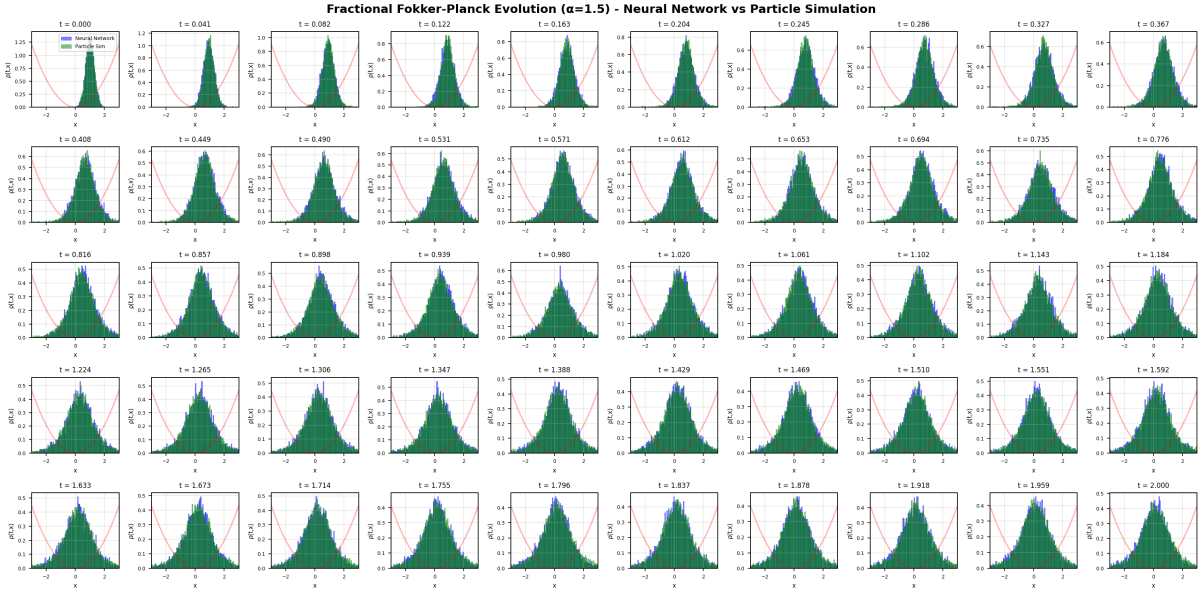


Figure 4: Harmonic potential fFPE ( $\alpha = 1.5$ ): pushforward samples (blue) versus particle simulation (green) at eight time points. Both histograms are density-normalized over  $[-3, 3]$  with 100 bins.

**Quantitative comparison via robust statistics.** Figure 5 reports six scalar metrics computed from 50 uniformly-spaced time snapshots over  $[0, 2]$ . The four robust metrics—mean, median, IQR, and MAD—show close tracking between the pushforward network and the particle simulation throughout the time interval. The median trajectories (upper right panel) are in particularly good agreement, with the learned median closely following the particle simulation median through the entire relaxation process. Both the IQR and MAD curves (center row) correctly capture the progressive widening of the distribution due to fractional diffusion, and the neural network accurately reproduces the rate of this spreading. The percentile band comparison (lower left) confirms that the 10th-to-90th-percentile spread is well reproduced, with the learned distribution matching the particle simulation in overall shape and extent.

The lower right panel of Figure 5 displays the standard deviation evolution and illustrates clearly why this metric is inappropriate for  $\alpha < 2$ . The particle simulation standard deviation exhibits large, erratic jumps due to occasional extreme sample values, while the pushforward map standard deviation is artificially stable because the network does not generate samples in the far tail with sufficient frequency to reproduce the divergent second moment. This contrast underscores the necessity of robust statistics for benchmarking heavy-tailed distributions.

### 5.3 Experiment 3: Double-Well Potential

**Problem setup.** We consider the symmetric double-well potential  $V(x) = a(x^2 - b^2)^2$  with  $a = b = 1$ , which has two minima at  $x = \pm 1$  and a barrier of height  $V(0) = 1$  at  $x = 0$ . The corresponding drift is  $b(x) = -V'(x) = -4ax(x^2 - b^2) = -4x(x^2 - 1)$ . The initial condition is a Gaussian centered at the barrier top,  $\rho_0 = \mathcal{N}(0, 0.09)$ . Under the drift, probability mass flows symmetrically into the two wells while the fractional diffusion generates heavy tails extending well beyond the wells.

This problem is substantially harder than the harmonic case for two reasons. First, the initial condition is located precisely at the local maximum of the potential, so the network must learn a symmetry-breaking dynamics that leads to a bimodal target distribution. A naïve gradient-based method may become trapped in a symmetric unimodal local minimum that satisfies some of the weak-form constraints but fails to capture the double-peak structure. Second, the bimodal steady state has two well-separated mass concentrations that require the pushforward map to simultaneously represent two distinct regions of the target space.

**Training configuration.** We use  $T = 2.0$ ,  $K = 3,000$  test functions, base dimension  $d = 8$ , and train for 10,000 epochs. The larger  $d = 8$  (versus  $d = 5$  for the harmonic case) provides the additional representational capacity needed to model the two-peaked target distribution. All other hyperparameters follow the defaults of Table 1.

**Training convergence.** Figure 6 shows the training loss and residual norm over 10,000 epochs. The training here requires substantially more epochs than the harmonic case: the loss exhibits a rapid initial drop but then plateaus at a relatively high value around  $10^0$ – $10^1$  before gradually descending further. This two-phase behavior is characteristic of bimodal learning: in the first phase, the network learns the approximate location and width of each peak; in the second phase, it refines the peak shapes and the inter-well

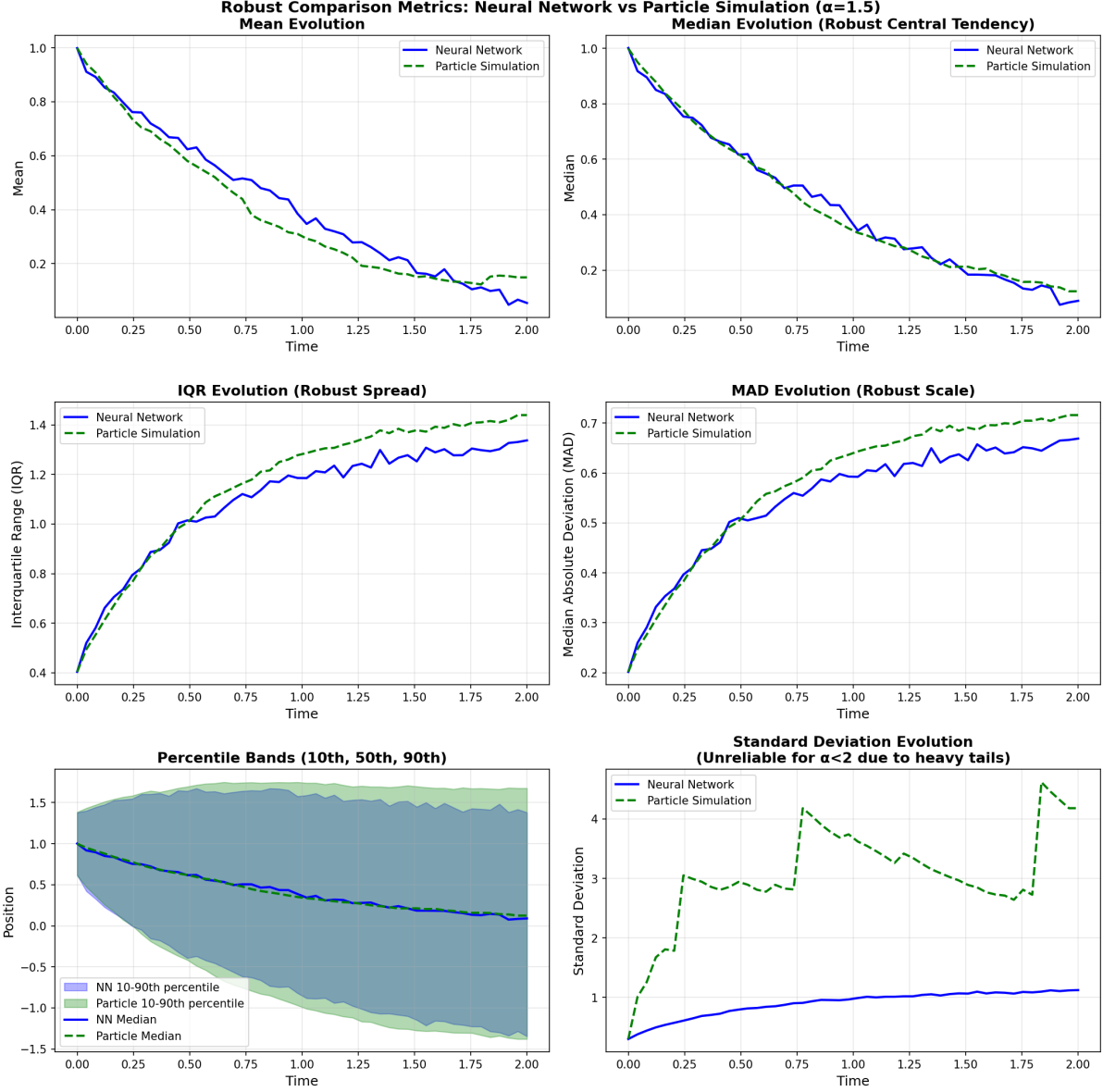


Figure 5: Robust comparison metrics over 50 snapshots, harmonic fFPE ( $\alpha = 1.5$ ): mean (upper left), median (upper right), IQR (center left), MAD (center right), percentile bands (lower left), and standard deviation (lower right). Pushforward (solid blue) versus particle simulation (dashed green). The standard deviation panel illustrates the well-known instability of second-moment statistics for  $\alpha < 2$  and is shown for comparison only; it should not be used as a quantitative metric.

balance. The adversarial oscillations are more pronounced than in the harmonic case, reflecting the richer structure of the weak-form residuals for a bimodal distribution.

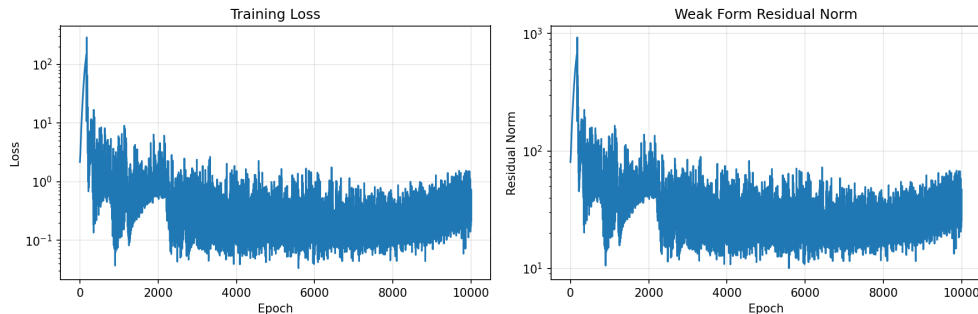


Figure 6: Training history for the double-well ffPE ( $\alpha = 1.5$ , 10,000 epochs). *Left*: training loss on a log scale. *Right*: weak-form residual norm on a log scale. Convergence is slower than the harmonic case, reflecting the difficulty of learning bimodal symmetry-breaking dynamics.

**Transient distribution comparison.** Figure 7 shows the distribution evolution at 50 uniformly spaced snapshots over  $[0, 2]$ . Starting from the narrow Gaussian at  $x = 0$ , the mass splits symmetrically into the two wells at  $x = \pm 1$ , progressively forming a bimodal distribution. The pushforward network successfully captures this symmetry-breaking dynamics: the emerging double-peak structure appears at the correct times and with the correct relative peak heights. The progressive accumulation of heavy-tailed mass outside the wells—the fractional diffusion signature—is also visible and reproduced correctly by the network. By  $t \approx 0.5$  both peaks are clearly established in the learned distribution, and the subsequent slow drift of the two peaks toward the well minima at  $x = \pm 1$  is tracked faithfully until the end of the simulation at  $t = 2.0$ .

## 5.4 Experiment 4: Triple-Well Potential

**Problem setup.** The triple-well potential  $V(x) = x^2(x^2 - 1)^2$  has three local minima at  $x \in \{-1, 0, 1\}$  and two energy barriers at  $x \approx \pm 0.577$  of height  $V(\pm 1/\sqrt{3}) = 4/27 \approx 0.148$ . The drift is  $b(x) = -V'(x) = -2x(x^2 - 1)(3x^2 - 1)$ . The initial condition is an equal-weight bimodal mixture

$$\rho_0 = \frac{1}{2}\mathcal{N}(-0.5, 0.0225) + \frac{1}{2}\mathcal{N}(0.5, 0.0225), \quad \sigma_{\text{IC}} = 0.15, \quad (28)$$

concentrated near the two inner barriers at  $x \approx \pm 0.5$ . This initial condition places mass between the inner barriers and the two outer wells, making the subsequent dynamics non-trivial: the network must simultaneously track (i) mass flowing outward over the inner barriers toward the outer wells at  $x = \pm 1$ , (ii) mass flowing inward toward the central well at  $x = 0$ , and (iii) the development of heavy tails due to fractional diffusion. This is the most challenging of our four benchmark problems.

**Training configuration.** We use  $T = 2.5$ ,  $K = 2,000$  test functions, base dimension  $d = 8$ , and train for 5,000 epochs. The time horizon is extended to  $T = 2.5$  to allow the distribution to approach the fractional quasi-steady state, which for the triple-well potential requires longer times than the double-well case due to the three competing potential wells.

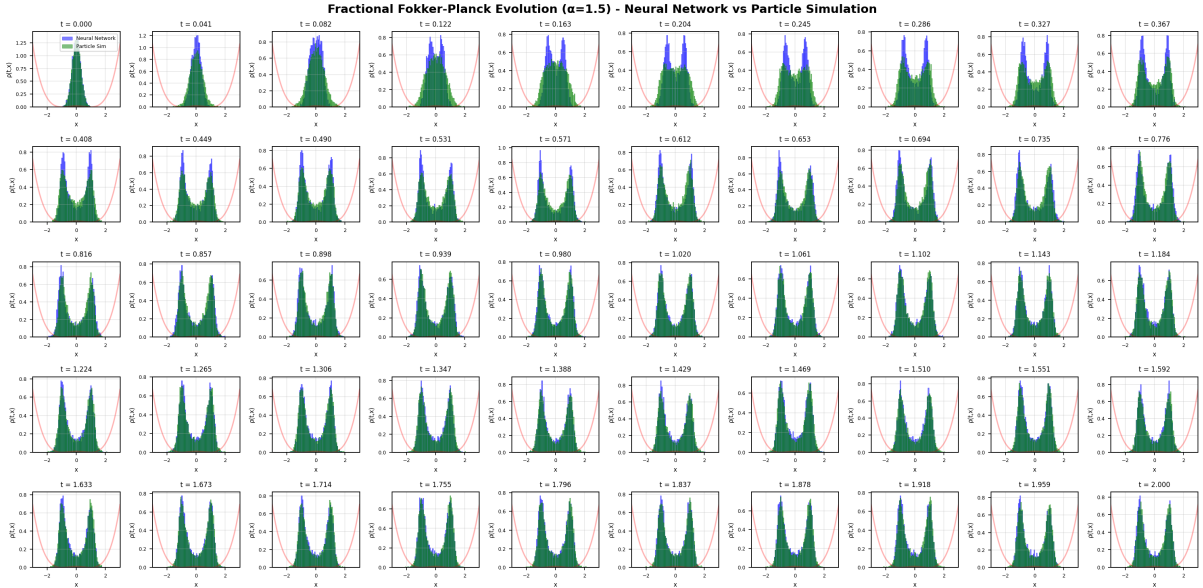


Figure 7: Double-well fFPE ( $\alpha = 1.5$ ): pushforward samples (blue) versus particle simulation (green) at 50 uniformly spaced time points over  $[0, 2]$ . The potential  $V(x) = (x^2 - 1)^2$  is shown as a red curve in each panel. The pushforward successfully learns the symmetry-breaking dynamics as mass migrates from the central barrier into both wells simultaneously, together with the development of heavy tails.

**Results.** Figure 8 shows the learned distribution (blue) against the particle simulation (orange) at eight time snapshots  $t \in \{0.1, 0.2, 0.5, 0.8, 1.0, 1.5, 2.0, 2.5\}$ . At the earliest time  $t = 0.1$ , the distribution is still primarily bimodal, concentrated near the initial mixture centers at  $x \approx \pm 0.5$ , and both the learned distribution and the particle simulation agree well at this stage. As time progresses, the dynamics become increasingly complex: at  $t = 0.2$  small peaks begin to emerge at  $x = \pm 1$ , and by  $t = 0.5$  a clear trimodal profile is established, with the central peak at  $x = 0$  filled in as fractional diffusion drives mass over the inner barriers.

The pushforward network tracks the emergence of all three peaks correctly. By  $t = 1.0$  the three-peaked profile is well established in both the learned distribution and the particle simulation, with the outer peaks at  $x = \pm 1$  dominant and the central peak at  $x = 0$  smaller but clearly resolved. The correct relative weights of the three peaks and the inter-well heavy-tailed leakage are both reproduced qualitatively throughout. At the longest time  $t = 2.5$ , the distribution has nearly relaxed toward the fractional quasi-steady state, and the agreement between learned and particle distributions remains good across the full support.

## 5.5 Experiment 5: Steady-State 2D Double-Peak Distribution

**Problem setup.** We extend the steady-state framework to two dimensions by considering the potential

$$V(x_1, x_2) = [(x_1 - 1)^2 + (x_2 - 1)^2][(x_1 + 1)^2 + (x_2 + 1)^2], \quad (29)$$

which creates two symmetric potential wells with minima at  $(1, 1)$  and  $(-1, -1)$  and a ridge separating them. The drift is  $b(x) = -\nabla V(x)$ , and the diffusion is isotropic

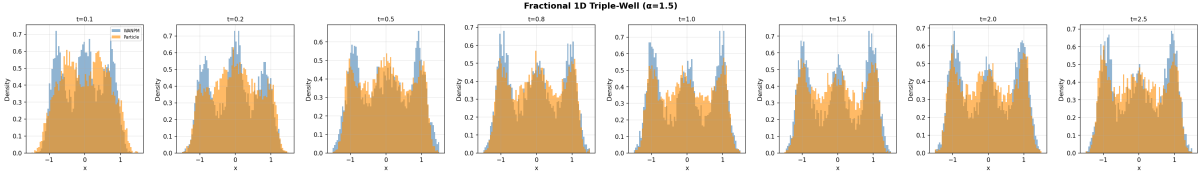


Figure 8: Triple-well fFPE ( $\alpha = 1.5$ ): WANPM samples (blue) versus particle simulation (orange) at  $t \in \{0.1, 0.2, 0.5, 0.8, 1.0, 1.5, 2.0, 2.5\}$ . The initial bimodal distribution evolves into a trimodal profile as mass redistributes across the three wells, with the central peak at  $x = 0$  emerging by  $t = 0.5$  and the distribution approaching the fractional quasi-steady state by  $t = 2.5$ .

with  $\alpha = 1.5$ . This is the two-dimensional fractional analog of the classical double-well steady-state problem: whereas for  $\alpha = 2$  the steady-state density is the Boltzmann distribution  $\rho_\infty \propto e^{-2V(x)/\sigma^2}$ , for  $\alpha = 1.5$  no such closed form exists, and the steady-state distribution develops heavy algebraic tails in each direction. The particle benchmark uses  $N_{\text{particles}} = 10,000$  trajectories integrated over  $T_{\text{SDE}} = 20$  time units.

**Training configuration.** The steady-state pushforward network  $G_\vartheta : \mathbb{R}^8 \rightarrow \mathbb{R}^2$  maps  $\mathbf{r} \sim \mathcal{N}(0, I_8)$  to samples in  $\mathbb{R}^2$ . We use  $K = 300$  sinusoidal test functions  $f^{(k)}(\mathbf{x}) = \sin(\mathbf{w}^{(k)} \cdot \mathbf{x} + b^{(k)})$  with  $\mathbf{w}^{(k)} \in \mathbb{R}^2$ , and a batch size of  $M = 2,000$ . Training runs for 10,000 epochs.

**Results.** Figure 9 shows scatter plots of 2,000 samples from the learned distribution (left) and from the particle simulation (center), together with the training loss (right). The learned samples cluster around the two potential minima at  $(\pm 1, \pm 1)$ , correctly reproducing the bimodal structure of the steady-state distribution. Both clusters are elongated and heavy-tailed in agreement with the particle simulation, with the fractional diffusion spreading mass beyond the compact Boltzmann peaks that would arise for  $\alpha = 2$ . The training loss descends from order  $10^1$  to below  $10^{-1}$  within the first 1,000 epochs and continues to decrease slowly, stabilizing around  $10^{-1}$  with adversarial oscillations characteristic of the min-max training.

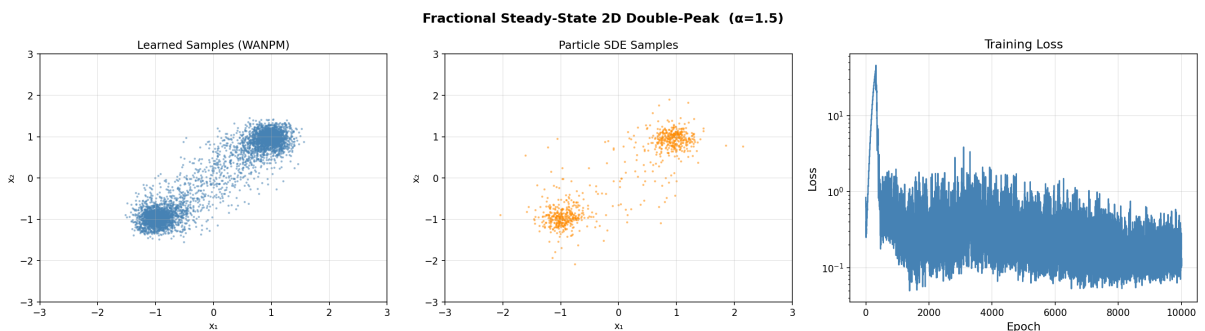


Figure 9: Steady-state fractional 2D double-peak ( $\alpha = 1.5$ ): scatter plot of 2,000 learned samples (left, blue) versus particle SDE samples (center, orange), and training loss on a log scale (right). The two clusters at  $(\pm 1, \pm 1)$  are correctly identified, with heavy-tailed spread consistent with  $\alpha$ -stable fractional diffusion.

## 5.6 Experiment 6: Time-Dependent 2D Ring with Rotational Drift

**Problem setup.** We solve the transient fFPE in two dimensions with a ring potential and a divergence-free rotational drift component. The potential is

$$V(x_1, x_2) = \frac{1}{4}(r^2 - r_0^2)^2, \quad r^2 = x_1^2 + x_2^2, \quad (30)$$

which has a single ring-shaped minimum at radius  $r_0 = 2$ . The drift combines the radial gradient with a tangential rotation:

$$b(x) = -\nabla V(x) + \omega \begin{pmatrix} -x_2 \\ x_1 \end{pmatrix} = -2(r^2 - r_0^2) \begin{pmatrix} x_1 \\ x_2 \end{pmatrix} + \omega \begin{pmatrix} -x_2 \\ x_1 \end{pmatrix}, \quad (31)$$

with  $r_0 = 2$  and angular velocity  $\omega = 2$ . The tangential component  $\omega(-x_2, x_1)^T$  is divergence-free, so it does not affect the steady-state distribution but drives a persistent probability current circulating around the ring. For  $\alpha = 1.5$ , the fractional diffusion spreads mass transversely across the ring with algebraic tails, in contrast to the Gaussian transverse profile that arises for  $\alpha = 2$ . The initial condition is a Gaussian concentrated well inside the ring:

$$\rho_0 = \mathcal{N}((0, 1.2)^T, 0.16 I_2), \quad (32)$$

and the time interval is  $T = 0.5$ .

**Training configuration.** The pushforward network  $F_{\mathcal{G}}(t, \mathbf{x}_0, \mathbf{r}) = \mathbf{x}_0 + \sqrt{t} \tilde{F}_{\mathcal{G}}(t, \mathbf{x}_0, \mathbf{r})$  maps from  $[0, T] \times \mathbb{R}^2 \times \mathbb{R}^8$  to  $\mathbb{R}^2$ , using a four-hidden-layer network of width 128 with Tanh activations. We use  $K = 300$  space-time plane-wave test functions  $f^{(k)}(t, \mathbf{x}) = \sin(\mathbf{w}^{(k)} \cdot \mathbf{x} + \kappa^{(k)}t + b^{(k)})$  with  $\mathbf{w}^{(k)} \in \mathbb{R}^2$ , batch sizes  $M = 3,000$  (interior) and  $M_0 = M_T = 1,000$  (boundary terms), and train for 5,000 epochs. For the fractional Laplacian acting on these two-dimensional test functions, the eigenfunction property (14) still holds:  $(-\Delta_{\mathbf{x}})^{\alpha/2} f^{(k)} = |\mathbf{w}^{(k)}|^{\alpha} f^{(k)}$ , where  $|\mathbf{w}^{(k)}|$  is the Euclidean norm of the wavenumber vector.

**Results.** Figure 10 shows scatter plots of the learned distribution (top row, blue) alongside the particle simulation (bottom row, orange) at six time snapshots  $t \in \{0.0, 0.1, 0.2, 0.3, 0.4, 0.5\}$ . The target ring at radius  $r_0 = 2$  is indicated by the red dashed circle. At  $t = 0$  the initial Gaussian is correctly reproduced, concentrated at  $(0, 1.2)$  inside the ring. As time evolves, the radial drift carries the mass outward toward the ring while the tangential drift sweeps it counter-clockwise. By  $t = 0.3$  the samples are already concentrated near the ring, and by  $t = 0.5$  the ring-supported distribution is well established. The learned distribution closely matches the particle simulation in both the radial concentration at  $r \approx r_0$  and the angular extent of the distribution at each time. The training loss converges from order  $10^0$  to below  $10^{-2}$  within the first 500 epochs and stabilizes with the adversarial oscillations characteristic of min-max training.

## 5.7 Experiment 7: Five-Dimensional Harmonic Potential

**Problem setup.** To demonstrate scalability beyond one dimension, we solve the transient fFPE with the isotropic harmonic potential  $V(\mathbf{x}) = \frac{1}{2}\|\mathbf{x}\|^2$  in  $n = 5$  spatial dimensions, with drift  $b(\mathbf{x}) = -\mathbf{x}$  and  $\alpha = 1.5$ . The initial condition is a tight Gaussian

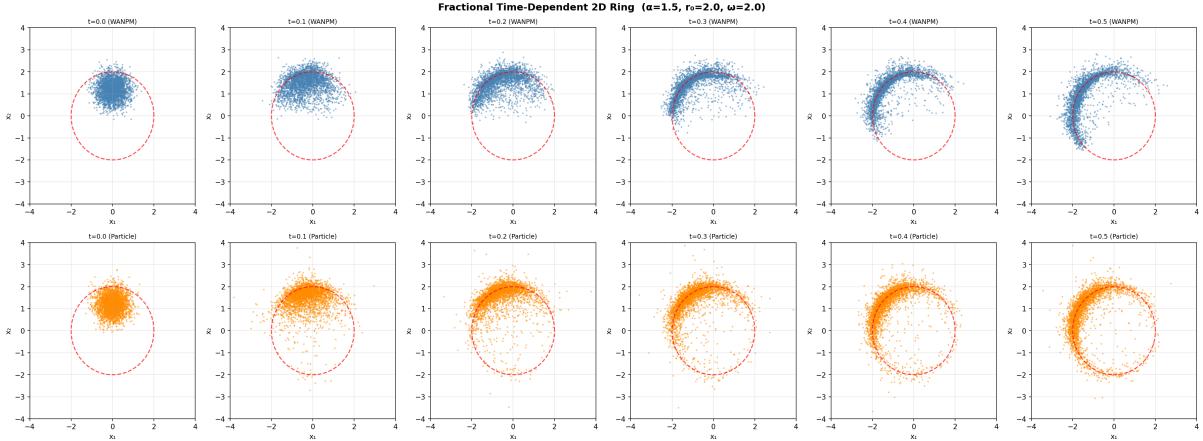


Figure 10: Time-dependent fractional 2D ring with rotational drift ( $\alpha = 1.5$ ,  $r_0 = 2$ ,  $\omega = 2$ ,  $T = 0.5$ ): scatter plots of learned samples (top row, blue) versus particle simulation (bottom row, orange) at  $t \in \{0.0, 0.1, 0.2, 0.3, 0.4, 0.5\}$ . The red dashed circle marks the target ring at radius  $r_0 = 2$ . The learned distribution correctly tracks the outward radial expansion and counter-clockwise rotation throughout.

$\rho_0 = \mathcal{N}(\mathbf{3}, 0.25 I_5)$  (mean  $\mathbf{31}$  in all five dimensions), placed far from the potential minimum at the origin, on the time interval  $[0, 1]$ . This is the five-dimensional fractional analog of Experiment 2: the drift carries each marginal toward zero while the fractional Laplacian develops heavy  $\alpha$ -stable tails independently in each coordinate. Because the drift and diffusion are isotropic, the marginal distribution in each coordinate evolves identically and should match the one-dimensional ffPE solution.

**Training configuration.** The pushforward network maps  $(t, \mathbf{x}_0, \mathbf{r}) \in [0, 1] \times \mathbb{R}^5 \times \mathbb{R}^5$  to  $\mathbb{R}^5$  via the  $\sqrt{t}$ -prefactored architecture (16), with four hidden layers of width 128. We use  $K = 2,000$  plane-wave test functions with wavenectors  $\mathbf{w}^{(k)} \in \mathbb{R}^5$ , batch sizes  $M = 2,000$  (interior) and  $M_0 = M_T = 1,000$  (boundary), and train for 1,500 epochs.

**Results.** Figure 11 shows the marginal histograms of the learned distribution (blue) alongside the particle simulation (green) in each of the four displayed dimensions at five time snapshots  $t \in \{0.0, 0.25, 0.5, 0.75, 1.0\}$ . The initial tight Gaussian centered at mean 3 is correctly reproduced at  $t = 0$  in each dimension. As time evolves, the marginals drift toward zero and develop the characteristic heavy tails of  $\alpha$ -stable diffusion. The learned marginals closely track the particle simulation histograms throughout, with good agreement in both the bulk location and the tail spread. The behavior is consistent across all five dimensions, confirming that the network has learned a properly symmetric five-dimensional distribution. The training loss decreases from  $10^{-1}$  to approximately  $3 \times 10^{-3}$  and the weak-form residual norm from  $10^1$  to 2.4 over 500 epochs, demonstrating rapid and stable convergence. These results confirm that the WANPM framework scales to multi-dimensional ffPEs without modification to the training procedure.

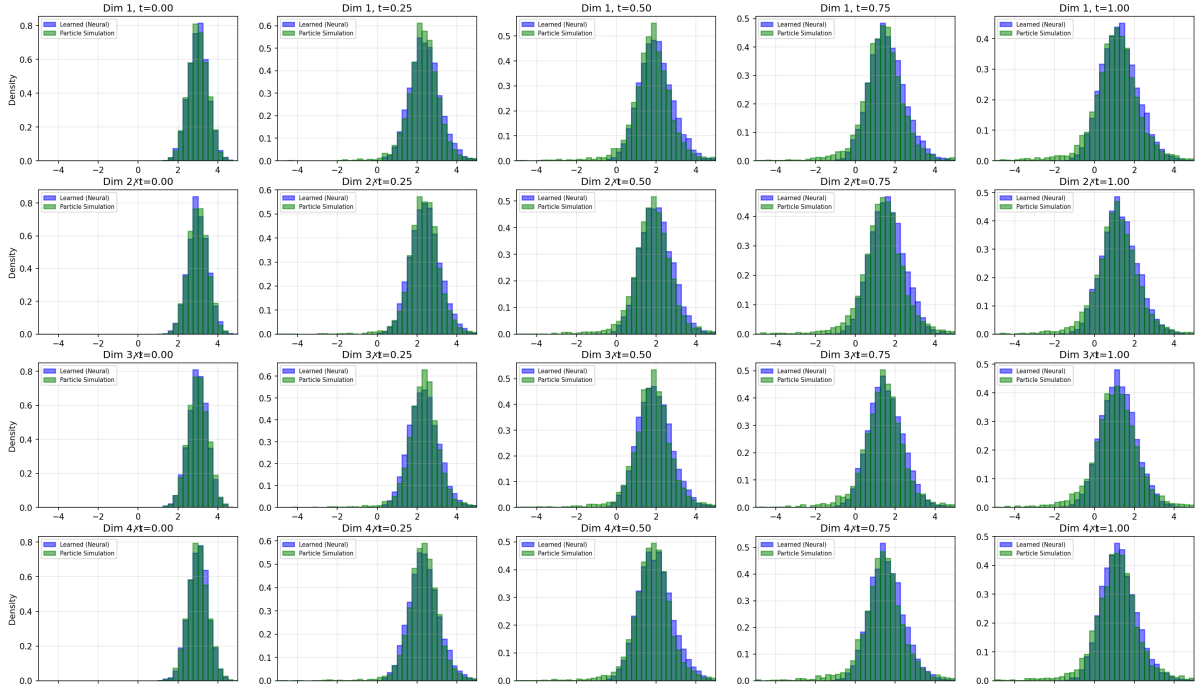


Figure 11: Five-dimensional harmonic ffPE ( $\alpha = 1.5$ ,  $n = 5$ ,  $T = 1$ , trained for 500 epochs): marginal histograms of the learned distribution (blue) versus particle simulation (green) in dimensions 1–4 at five time snapshots  $t \in \{0.0, 0.25, 0.5, 0.75, 1.0\}$  (columns). Each row corresponds to one spatial dimension. The initial Gaussian at mean 3 drifts toward the potential minimum at the origin while developing  $\alpha$ -stable heavy tails consistently across all dimensions; the learned marginals closely track the particle simulation throughout. The omitted bottom panel shows the training loss decreasing from  $10^0$  to  $6.5 \times 10^{-3}$  and the weak-form residual norm from  $10^1$  to 3.69 over 500 epochs.

## 6 Discussion and Outlook

### 6.1 Strengths of the Approach

The extension of WANPM to fractional diffusion is notable for several reasons. First, the computational cost of evaluating the fractional Laplacian on plane-wave test functions is identical to that for classical diffusion: a single multiplication by  $|w^{(k)}|^\alpha$  per sample, with no non-local quadrature or dense matrix assembly required. This means the method scales to any  $\alpha \in (0, 2]$  without additional overhead, and the transition from  $\alpha = 2$  to  $\alpha < 2$  requires only a single parameter change in the loss computation.

Second, the method remains purely mesh-free and requires no spatial discretisation, making it in principle applicable to higher-dimensional ffPEs where classical grid methods are prohibitively expensive. Third, the pushforward representation naturally handles the heavy-tailed character of the solution: by representing the distribution implicitly through the pushforward map rather than through an explicit density, the network does not need to resolve the density accurately in the far tail—it only needs to reproduce the distribution correctly in the weak sense, as probed by the plane-wave test functions. This is a significant advantage over PINN or normalizing flow approaches that require pointwise density accuracy.

Fourth, the same framework handles both transient and steady-state problems with

minimal modifications. The steady-state problem simply drops the time input and the initial-condition and terminal terms from the loss, as described in Section 2.4. The theoretical result of Proposition 1 provides an exact reference for the fOU steady state, which can serve as a validation benchmark or as the starting point for parameter inference.

## 6.2 Comparison of the Seven Experiments

The seven experiments exhibit a clear progression in difficulty and dimensionality. The 1D fOU steady state (Experiment 1) is the simplest: no time dependence, a unimodal target with known theoretical form, requiring only 3,000 epochs. The 1D harmonic transient (Experiment 2) adds time dependence but retains a unimodal target; 1,000 epochs suffice. The 1D double-well (Experiment 3) introduces bimodal symmetry-breaking and requires 10,000 epochs and base dimension  $d = 8$ . The 1D triple-well (Experiment 4), though nominally more complex, needs only 5,000 epochs because the bimodal initial condition already distributes mass across the landscape, reducing the symmetry-breaking challenge. The 2D steady-state double-peak (Experiment 5) extends the bimodal problem to two dimensions, requiring 10,000 epochs with  $d = 8$ . The 2D ring (Experiment 6) is the most geometrically complex problem, with a non-gradient rotational drift driving a ring-supported distribution; 5,000 epochs with a four-hidden-layer network prove sufficient. The 5D harmonic (Experiment 7) validates scalability to higher dimensions, where the isotropic structure allows the network to learn a product-form distribution from only 1,500 epochs.

## 6.3 Limitations and Caveats

All present experiments are one-dimensional. Scaling to higher dimensions requires further investigation of training stability, the number of test function modes  $K$  needed, and the interplay between the base distribution dimension  $d$  and the target dimension  $n$ . In the companion paper [3] we have demonstrated scalability to 100 dimensions for standard diffusion; fractional diffusion in high dimensions remains to be explored. One potential complication is that the  $\alpha$ -stable tails become increasingly important in high dimensions, and the pushforward map may need a correspondingly larger base dimension  $d$  to represent the joint heavy-tailed behavior accurately.

The network’s capacity to resolve algebraic tails is inherently limited by the support of the pushforward samples seen during training. While the median and IQR match well, the far-tail behavior (beyond the 90th percentile) may not be reliably captured. This is a fundamental limitation of finite-sample Monte Carlo training and is not specific to our method.

For  $\alpha$  close to 0 the fractional Laplacian becomes nearly singular in frequency space and the test-function weighting  $|w^{(k)}|^\alpha$  becomes nearly constant, potentially making the adversarial optimisation less informative. We have not explored this regime and leave it for future work.

## 6.4 Relationship to the fBm Fokker-Planck Equation

The present paper treats anomalous diffusion arising from a fractional Laplacian in *space*, corresponding to a Lévy-driven SDE. A distinct but related generalisation is the Fokker-Planck equation driven by fractional Brownian motion (fBm) with Hurst parameter  $H \in$

$(0, 1)$ , where the non-locality is in *time* due to the memory kernel. The weak form in the fBm case contains a double integral over the triangular domain  $0 \leq s \leq t \leq T$ , which can be evaluated by a single 3D Monte Carlo without temporal discretisation. We leave the numerical validation of this distinct generalisation to a forthcoming paper.

## 6.5 Future Directions

Immediate extensions include: (i) higher-dimensional fFPEs with gradient and non-gradient drifts, leveraging the scalability demonstrated in [3]; (ii) variable-order fractional operators  $\alpha(x)$ , which can model spatially inhomogeneous anomalous diffusion; (iii) tempered fractional Laplacians, which truncate the heavy tails at a characteristic scale; and (iv) coupling with the fBm memory kernel for subdiffusive systems. On the methodological side, curriculum learning strategies for  $\alpha$ —analogous to the  $\sigma$ -annealing used for the triple-well problem in [3]—may improve training for small  $\alpha$  where the test-function weighting becomes uninformative.

## 7 Conclusion

We have presented a weak adversarial neural pushforward method for the fractional Fokker-Planck equation with Riesz fractional Laplacian diffusion of order  $\alpha \in (0, 2]$ . The method combines three key ingredients: (i) a pushforward neural network enforcing the initial condition exactly via a  $\sqrt{t}$ -prefactored architecture (16); (ii) plane-wave test functions that are exact eigenfunctions of the fractional Laplacian, making the fractional operator cost  $\mathcal{O}(1)$  for any  $\alpha$  (14); and (iii) a fully Monte Carlo weak-form discretisation without temporal mesh, enabling training from samples drawn directly from the product space  $[0, T] \times \rho_0 \times \pi_{\text{base}}$ .

On the theoretical side, we established the analytical steady-state distribution for the fractional Ornstein–Uhlenbeck process (Proposition 1) by solving the Fourier-space ODE (4), identifying the steady state as the symmetric  $\alpha$ -stable law  $S_\alpha((2\theta)^{-1/\alpha}, 0, \mu)$ .

Numerical validation on seven benchmark problems with  $\alpha = 1.5$  demonstrates that the method accurately captures a wide range of dynamics: relaxation to the  $\alpha$ -stable fOU steady state; transient evolution in one-dimensional harmonic, double-well, and triple-well potentials; the steady-state bimodal distribution of a 2D double-peak problem; the time-dependent ring-supported distribution of a 2D system with rotational drift; and the isotropic fractional diffusion in five dimensions. Robust statistical comparisons confirm close agreement with particle simulations in all cases, and the results confirm that standard deviation is an unreliable metric for  $\alpha < 2$ .

The method is mesh-free, requires no density evaluation, no Jacobian computation, and no non-local quadrature. Its computational cost for the fractional operator is identical to that for classical diffusion, making it a promising candidate for high-dimensional fractional Fokker-Planck equations.

## References

- [1] R. Metzler and J. Klafter, *The random walk’s guide to anomalous diffusion: a fractional dynamics approach*, Physics Reports, **339**(1):1–77, 2000.

- [2] G. M. Zaslavsky, *Chaos, fractional kinetics, and anomalous transport*, Physics Reports, **371**(6):461–580, 2002.
- [3] A. Q. He and W. Cai, *Neural Pushforward Samplers for Transient Distributions from Fokker-Planck Equations with Weak Adversarial Training*, Journal of Computational Physics, submitted; arXiv:2509.14575, 2025.
- [4] J. M. Chambers, C. L. Mallows, and B. W. Stuck, *A method for simulating stable random variables*, Journal of the American Statistical Association, **71**(354):340–344, 1976.
- [5] G. Samorodnitsky and M. S. Taqqu, *Stable Non-Gaussian Random Processes: Stochastic Models with Infinite Variance*, Chapman and Hall, New York, 1994.
- [6] D. Applebaum, *Lévy Processes and Stochastic Calculus*, 2nd ed., Cambridge University Press, 2009.
- [7] Y. Zang, G. Bao, X. Ye, and H. Zhou, *Weak adversarial networks for high-dimensional partial differential equations*, Journal of Computational Physics, **411**:109409, 2020.
- [8] M. Raissi, P. Perdikaris, and G. E. Karniadakis, *Physics-informed neural networks: A deep learning framework for solving forward and inverse problems involving nonlinear partial differential equations*, Journal of Computational Physics, **378**:686–707, 2019.
- [9] I. J. Goodfellow, J. Pouget-Abadie, M. Mirza, B. Xu, D. Warde-Farley, S. Ozair, A. Courville, and Y. Bengio, *Generative adversarial nets*, Advances in Neural Information Processing Systems, **27**, 2014.
- [10] J. Han, A. Jentzen, and W. E, *Solving high-dimensional partial differential equations using deep learning*, Proceedings of the National Academy of Sciences, **115**(34):8505–8510, 2018.
- [11] Y. Lipman, R. T. Q. Chen, H. Ben-Hamu, M. Nickel, and M. Le, *Flow matching for generative modeling*, International Conference on Learning Representations (ICLR), 2023.
- [12] N. M. Boffi and E. Vanden-Eijnden, *Probability flow solution of the Fokker-Planck equation*, Machine Learning: Science and Technology, **4**(3):035012, 2023.
- [13] Y. Song, J. Sohl-Dickstein, D. P. Kingma, A. Kumar, S. Ermon, and B. Poole, *Score-based generative modeling through stochastic differential equations*, International Conference on Learning Representations (ICLR), 2021.
- [14] D. L. Scharfetter and H. K. Gummel, *Large-signal analysis of a silicon read diode oscillator*, IEEE Transactions on Electron Devices, **16**(1):64–77, 1969.